E x B electron drift instability in Hall thrusters: Particle-in-cell simulations vs. theory

Jean-Pierre Boeuf, Laurent Garrigues

E × B electron drift instability in Hall thrusters: Particle-in-cell simulations vs. theory

J. P. Boeuf, and L. Garrigues

Articles you may be interested in

Electron energy distribution function in a low-power Hall thruster discharge and near-field plume
Physics of Plasmas **25**, 061205 (2018); 10.1063/1.5017578

Ion velocity analysis of rotating structures in a magnetic linear plasma device
Physics of Plasmas **25**, 061203 (2018); 10.1063/1.5019448

Particle-in-cell modeling of laser Thomson scattering in low-density plasmas at elevated laser intensities
Physics of Plasmas **25**, 053513 (2018); 10.1063/1.5029820

Tutorial: Physics and modeling of Hall thrusters
Journal of Applied Physics **121**, 011101 (2017); 10.1063/1.4972269

Laboratory space physics: Investigating the physics of space plasmas in the laboratory
Physics of Plasmas **25**, 055501 (2018); 10.1063/1.5025421

Anomalous electron transport in Hall-effect thrusters: Comparison between quasi-linear kinetic theory and particle-in-cell simulations
Physics of Plasmas **25**, 061202 (2018); 10.1063/1.5017626

E × B electron drift instability in Hall thrusters: Particle-in-cell simulations vs. theory

J. P. Boeuf[a] and L. Garrigues

LAPLACE, Université de Toulouse, CNRS, INPT, UPS, 118 Route de Narbonne, 31062 Toulouse, France

The $E \times B$ Electron Drift Instability ($E \times B$ EDI), also called Electron Cyclotron Drift Instability, has been observed in recent particle simulations of Hall thrusters and is a possible candidate to explain anomalous electron transport across the magnetic field in these devices. This instability is characterized by the development of an azimuthal wave with wavelength in the mm range and velocity on the order of the ion acoustic velocity, which enhances electron transport across the magnetic field. In this paper, we study the development and convection of the $E \times B$ EDI in the acceleration and near plume regions of a Hall thruster using a simplified 2D axial-azimuthal Particle-In-Cell simulation. The simulation is collisionless and the ionization profile is not-self-consistent but rather is given as an input parameter of the model. The aim is to study the development and properties of the instability for different values of the ionization rate (i.e., of the total ion production rate or current) and to compare the results with the theory. An important result is that the wavelength of the simulated azimuthal wave scales as the electron Debye length and that its frequency is on the order of the ion plasma frequency. This is consistent with the theory predicting destruction of electron cyclotron resonance of the $E \times B$ EDI in the non-linear regime resulting in the transition to an ion acoustic instability. The simulations also show that for plasma densities smaller than under nominal conditions of Hall thrusters the field fluctuations induced by the $E \times B$ EDI are no longer sufficient to significantly enhance electron transport across the magnetic field, and transit time instabilities develop in the axial direction. The conditions and results of the simulations are described in detail in this paper and they can serve as benchmarks for comparisons between different simulation codes. Such benchmarks would be very useful to study the role of numerical noise (numerical noise can also be responsible to the destruction of electron cyclotron resonance) or the influence of the period of the azimuthal domain, as well as to reach a better and consensual understanding of the physics. *Published by AIP Publishing.*
https://doi.org/10.1063/1.5017033

I. INTRODUCTION

Hall thrusters are gridless ion sources that are used for satellite propulsion. In a standard Hall thruster operating in the kW power range (e.g., 300 V, 4 A), xenon ions are extracted from a plasma without grids and accelerated to about 20 km/s and the thrust is on the order of 70 mN.[1,2]

In a Hall thruster, ions are accelerated by the large electric field generated in the quasineutral plasma due to the drop of electron conductivity induced by the presence of a magnetic barrier perpendicular to the path of electrons from the cathode to the anode. This external magnetic barrier is generated by coils or permanent magnets. The combination of the electric field E parallel to the discharge current with the perpendicular magnetic field B leads to a large electron drift in the $E \times B$ direction (Hall current). Good confinement of the electrons and an associated drop of electron conductivity can be achieved only if the Hall current does not hit a wall so the $E \times B$ direction must be closed on itself, i.e., must be in the azimuthal direction of a cylindrical configuration (Hall thrusters are "closed drift devices"[3]). In a Hall thruster, the electric field is axial and the magnetic field is

radial (see Fig. 1). The plasma is formed in a channel between two coaxial dielectric cylinders. Electrons are injected from an emissive cathode placed outside the exhaust plane, the anode being placed at the end of the channel. The residence time of electrons in the channel is increased by the magnetic barrier, allowing them to ionize the flow of neutral xenon atoms injected from the anode. Ionization efficiency is very good in Hall thrusters and more than 90% of the gas flow is ionized for applied voltages on the order of 200 V or more. Most Hall thrusters operate at current densities on the order of 1000 A/m². More details on the physics and operation of Hall thrusters can be found in Refs. 1 and 2.

An important feature of Hall thrusters is that ionization takes place immediately upstream of the region of large axial electric field, as can be seen in Fig. 1.

The ionization and acceleration regions are close together and even overlap, so that ions, which are essentially unmagnetized can be efficiently extracted from the plasma and accelerated by the axial electric field without collisions.

Because of the good ionization efficiency, the neutral density in the exhaust region of a Hall thruster is very small and electron transport across the magnetic field lines cannot be due to electron collisions with neutral atoms (the neutral density is too low by more than a factor of 10 to allow for
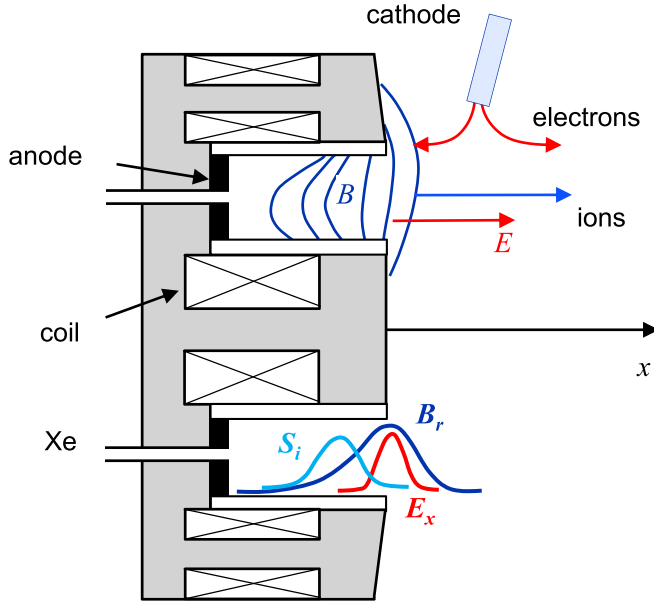
[a] Electronic mail: jpb@laplace.univ-tlse.fr

FIG. 1. Schematic of a Hall thruster. The curves labelled B_r, E_x, and S_i, show, respectively, the axial profiles along the mid channel axis, of the external radial magnetic field, axial electric field, and ionization rate (number of electron-ion pairs generated per unit volume per unit time).

classical, collisional cross-field transport, see Ref. 2 and references therein). Electron collisions with the channel walls and secondary electron emission as well as instabilities and turbulence could be responsible for electron transport through the magnetic field. Although Hall thrusters were originally developed more than 50 years ago and are in operation on a number of satellites, electron transport across the magnetic barrier ("anomalous" electron transport) is still not well understood. In the absence of reliable theory, the "anomalous" electron transport in the Hall thruster prevents the development of predictive simulation codes and the available fluid models of Hall thrusters use empirical coefficients to describe cross-field electron transport.[2]

In this paper, we use a 2D Particle-In-Cell (PIC) simulation to get insight into the physics of anomalous cross-field transport in Hall thrusters. The model is simplified in order to focus on the possible effects of instabilities and turbulence on cross-field electron transport. Ionization is not treated self-consistently (the ionization rate profile is given and is used as a parameter in the simulation), and the model is collisionless. Since instabilities and turbulence are likely to develop in the $E \times B$ direction because of the large difference between the electron and ion drift velocity in this direction, the simulation plane includes the axial and azimuthal directions (i.e., is perpendicular to the magnetic field), as in the self-consistent PIC simulations of Adam et al.[4,5] The simplified 2D model described in the present paper is used to compare the simulation results with those predicted by the theory of the $E \times B$ electron drift instability (or electron cyclotron drift instability) developed in the 1970s in the context of collisionless shocks in space plasmas[6–10] and more recently in the context of Hall thrusters.[6,7]

In Sec. II, we briefly summarize previous work on the $E \times B$ electron drift instability. In Sec. III, we describe the simplified 2D PIC model used in this paper. The simulation

results are presented and compared with the theory in Sec. IV. The question of accuracy and validity of the simulations is discussed in Sec. V.

II. PREVIOUS WORK ON THE $E \times B$ ELECTRON DRIFT INSTABILITY (EDI)

Two-dimensional Particle-In-Cell Monte Carlo Collisions (PIC MCC) simulations performed by Adam et al.[4] have shown that microturbulence can be responsible for anomalous electron transport in the $E \times B$ configuration of Hall thrusters. The 2D (axial-azimuthal) PIC MCC simulations showed the development of a small wavelength (in the mm range) azimuthal wave propagating at a velocity close to the ion acoustic velocity (i.e., with frequency in the 1–10 MHz range). Measurements of density fluctuations based on collective laser scattering[8] confirmed the presence of instabilities in the same range of wavelengths and frequencies but with smaller amplitudes than in the simulations.

This wave was clearly responsible, in these simulations, for cross-field electron transport in the exhaust region of the thruster (electron-wall interaction and secondary electron emission were not taken into account in the model) and the model was able to reproduce a number of experimental features of Hall thruster operations.

In order to understand the origin of this turbulence, the authors[4,9] derived the corresponding 2D dispersion relation and showed that, in the axial-azimuthal plane and assuming a zero wave vector along the magnetic field, the instability develops in packets of unstable modes ("comb of unstable modes developing for each $k_y V_d = n\Omega_{ce}$," where k_y is the azimuthal wave vector, V_d is the azimuthal electron drift velocity, Ω_{ce} is the electron cyclotron angular frequency, and n is an integer). The dispersion relation shows that the instability results from electron Bernstein waves which are Doppler-shifted towards low-frequencies by the high drift velocity V_d.

Cavalier et al.[6] presented a rather complete study of the 3D dispersion relation of the instability in the context of Hall thrusters. This dispersion relation is obtained by studying the development and growth of electrostatic waves in a uniform plasma with constant and perpendicular electric and magnetic fields E and B, with a hot magnetized electron beam drifting across the magnetic field and a non-magnetized cold ion beam. Linearizing Poisson's equation together with cold fluid equations for ions, and with the Vlasov kinetic equation for electrons, the following dispersion equation is obtained:[6,9]

$$1 + k^2\lambda_{De}^2 + g\left(\frac{\omega - k_y V_d}{\Omega_{ce}}, \left(k_x^2 + k_z^2\right)\rho_e^2, k_z^2\rho_e^2\right)$$
$$- \frac{k^2\lambda_{De}^2\omega_{pi}^2}{(\omega - k_x V_{i,b})^2} = 0, \tag{1}$$

where g is the Gordeev function:[6,10] $g(\Omega, X, Y) = \frac{\Omega}{2Y}e^{-X}\sum_{m=0}^{\infty} Z\left(\frac{\Omega - m}{\sqrt{2Y}}\right)I_m(X)$, λ_{De} is the electron Debye length, $V_d = E/B$ is the electron drift velocity, $\rho_e = v_{the}/\Omega_{ce}$ the electron Larmor radius, $v_{the} = \sqrt{k_B T_e/m}$ the electron

thermal velocity, ω_{pi} the ion plasma angular frequency, and $V_{i,b}$ the velocity of the ion beam. Z(z) is the plasma dispersion function and $I_m(X)$ is the modified Bessel function of the first kind. E and B are in the x and z directions, respectively.

Solutions of the 3D dispersion relation above, obtained by Cavalier et al. for conditions typical of Hall thrusters, are shown in Fig. 2. This figure shows that the comb of unstable modes found in the 2D, axial-azimuthal plane in Refs. 4 and 9 was smoothed out when a non-zero wave vector, k_z, was considered in the direction parallel to the magnetic field. One can see in Fig. 2 that, when the parameter k_z increases (even for very low values of $k_z\lambda_{De}$), the dispersion relation tends to an asymptotic curve corresponding to an ion acoustic instability which was termed as modified ion acoustic instability by Cavalier et al. The drift velocity V_d was identified as the mechanism of the instability, hence the name "$E \times B$ electron drift instability" ($E \times B$ EDI). It appears that the instability present in the PIC simulations of Hall thrusters is of the same nature as the instability studied in the 1970s in the context of space plasmas and collisionless shocks.[11–15]
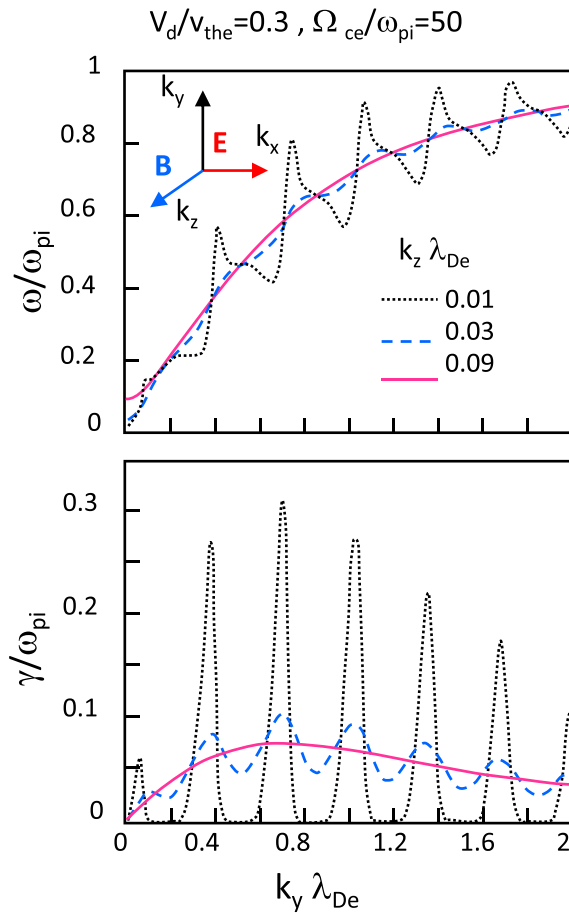

FIG. 2. Solutions of the 3D $E \times B$ EDI dispersion relation, adapted from Cavalier et al.[6] k_y and k_z are the wave vector components in the azimuthal and radial (parallel to B) directions, respectively; k_x is set to zero. ω and γ are the real part (angular frequency) and the imaginary part (growth rate) of the instability, respectively; ω_{pi} is the ion angular plasma frequency, $V_d = E/B$ the azimuthal electron drift velocity, v_{the} the electron thermal velocity, Ω_{ce} the electron cyclotron frequency, and λ_{De} the electron Debye length. The plotted results correspond to $\lambda_{De} = 8.3 \times 10^{-5}$ m and $\omega_{pi} = 5.1 \times 10^7$ rd/s, ($n = 2 \times 10^{17}$ m^{-3}, $T_e = 25$ eV, and $V_{i,b} = 16$ km/s).

This instability had been termed as "Electron cyclotron drift instability" or "beam-cyclotron instability" in the context of space plasmas. Following Cavalier et al., we will use the term $E \times B$ EDI because the instability here is driven by the large $E \times B$ electron drift (in the case of space plasmas the instability also resulted from a large difference between electron and ion drift but this difference was due to the presence of a beam of high energy ions).

Recent 1D and 2D particle models[7,16–19] of the $E \times B$ EDI in conditions of Hall thrusters seem to be consistent with the smoothing out of the electron cyclotron modes and the transition to an ion acoustic instability even though the z component of the wave vector is zero in these models. In their earlier, work on the beam cyclotron instability in space plasmas, Lampe et al.[14,15] showed that this instability, defined by a dispersion relation similar to Eq. (1) in the quasilinear regime, can evolve, at a sufficient level of turbulence, into the nonmagnetic ion-acoustic instability of Eq. (2) below.

Under these conditions, the individual cyclotron resonances are smeared out by anomalous wave-particle interaction (resonance broadening). This may be the reason for the transition to an ion acoustic wave in 1D and 2D particle models of Hall thrusters (there is however no consensus on this transition, see below). If the transition to the ion acoustic regime occurs, the ion acoustic instability evolves quasilinearly until saturation occurs, a possible saturation mechanism being ion-wave trapping.[7,14,15] The angular frequency and growth rate of the modified ion acoustic wave (valid for small values of λ_{De}/ρ_e and V_d/v_{the}) are given by (see Refs. 14, 15, 6, and 7)

$$\omega \approx k_x V_{i,b} + \frac{kc_s}{\left(1 + k^2\lambda_{De}^2\right)^{1/2}}, \quad \gamma \approx \sqrt{\frac{\pi m}{8M}}\frac{k_y V_d}{\left(1 + k^2\lambda_{De}^2\right)^{3/2}},$$

(2)

where c_s is the ion acoustic velocity.

The azimuthal wave number k_{max} giving the maximum growth rate can be obtained from $\partial\gamma/\partial k_y = 0$, which gives $k_{max} \approx (\lambda_{De}\sqrt{2})^{-1}$.

The corresponding wavelength is $\lambda_w \approx 2\pi\sqrt{2}\lambda_{De}$ (about nine times the electron Debye length). The angular frequency and growth rate at the maximum growth rate can then be calculated from the above equations. This gives, (for $k_x = 0$)

$$\omega_{max} \approx \frac{c_s}{\lambda_{De}\sqrt{3}} = \frac{\omega_{pi}}{\sqrt{3}}, \quad \text{and}$$

$$\gamma_{max} \approx \sqrt{\frac{\pi m}{54M}}\frac{V_d}{\lambda_{De}} = \sqrt{\frac{\pi}{54}}\omega_{pi}\frac{V_d}{v_{th}}.$$

(3)

The wave velocity in the azimuthal direction, $\omega_{max}/k_{max} \approx c_s\sqrt{2/3}$, is close to the ion acoustic velocity c_s, while the group velocity (in the axial direction) is $|\partial\omega/\partial k| \approx V_{i,b}$ (this group velocity indicates that the instability is convected at the velocity of the ion beam).

Using the trapping conditions discussed, e.g., by Degeling et al.,[20] and following Lafleur et al.,[18] the conditions

for saturation by ion trapping can be roughly estimated as follows. The velocity range within which an ion of azimuthal velocity v_y can be trapped is $-v_{tr} < (v_y - v_w) \leq v_{tr}$ where $v_w = \omega_{max}/k_{max}$ is the phase velocity of the instability and v_{tr} is the trapping velocity defined by

$$v_{tr} = 2\left(\frac{e\delta\tilde{\phi}}{M}\right)^{1/2}.$$

Saturation by ion wave trapping occurs if most ions are trapped by the wave. This leads to the following estimation of the rms amplitudes of the potential and electric field at saturation:[18]

$$\begin{cases} |\delta\phi_{rms}| = \dfrac{1}{4\sqrt{2}} \dfrac{M}{e}\left(\dfrac{\omega_{max}}{k_{max}}\right)^2 = \dfrac{T_e}{6\sqrt{2}} \\ |\delta E_{y,rms}| = k_{max}|\delta\phi_{rms}| = \dfrac{1}{12}\dfrac{T_e}{\lambda_{De}}. \end{cases} \quad (4)$$

Note finally that there is no consensus on the transition to an ion acoustic instability in the conditions of Hall thrusters. As said above, the results of particle simulations presented in Refs. 7, 16, 18, and 19 seem to be consistent with the scaling of the ion acoustic instability and saturation by ion wave trapping. However, in the recent 1D PC simulations of Janhunen et al.,[21] the authors claim that transition to the ion acoustic instability does not occur because the demagnetization condition due to nonlinear resonance broadening is not fulfilled for the electrons.

In this paper, we present 2D PIC simulations under simplified, but more realistic conditions than those of 1D PIC simulations. We compare the scaling of the results with those of the ion acoustic instability and we discuss the mechanism of saturation of the instability. Comparisons with the ion acoustic instability are only indicative since the simulations correspond to a strongly non-linear regime and to rather inhomogeneous plasma conditions.

III. PRINCIPLES OF THE 2D PIC MODEL

The 2D axial-azimuthal Particle-In-Cell model of a magnetic barrier described in the present paper is aimed at studying the $\boldsymbol{E} \times \boldsymbol{B}$ electron drift instability and associated anomalous electron transport under conditions close to those of a Hall thruster but with simplifying assumptions so as to allow faster parametric studies and direct comparisons with the theory above of the modified ion acoustic instability. The simplifying assumptions consist of decoupling electron transport from ionization and neutral transport (strong coupling leads to the low frequency ionization instability in a Hall thruster, not discussed here[2,22]) by assuming a given ionization source term (axial profile and intensity). The extracted ion current can be modified by changing the intensity of the ionization source term. Changing the position of the ionization source with respect to the magnetic barrier can also help understand questions associated with the concept of a double stage thruster (see Ref. 23).

Since instabilities and turbulence in $\boldsymbol{E} \times \boldsymbol{B}$ configurations are most likely to occur in the direction perpendicular

to the magnetic field, we consider (see Fig. 3) a 2D simulation domain in the axial-azimuthal plane (x,y). Electrons and ions are supposed to be collisionless but ionization is taken into account by imposing a given profile of the ionization rate, S(x), in the axial direction x (and uniform in the azimuthal direction). Only a section of the azimuthal direction, of width w is described in the simulation, and we assume periodic boundary conditions in this direction (the total length of the azimuthal direction would be too long—about 30 cm for a 1 kW thruster—for practical simulations).

The length of the domain in the axial direction is noted d. In most of the simulations presented here, w and d are, respectively, 1 and 2.5 cm (simulations with larger values of the dimension w in the azimuthal direction will also be reported to study the influence of the imposed periodicity in the azimuthal direction).

A. Charged particle injection

The electron current is injected along the emission line (Fig. 3) on the cathode side of the simulation domain (inside the domain, at a position very close to the right boundary, e.g., 1 mm from this boundary) to simulate the presence of an emitting cathode and to ensure current continuity and neutralization of the extracted ion beam. The number of electrons emitted from this location per unit time is equal to the number of electrons minus the number of ions reaching the anode per unit time, as indicated in the figure.

The axial profiles of the magnetic field, B, and of the given ionization rate, S, are shown in Fig. 4. The intensity and position of S with respect to the magnetic field can be modified to study the sensitivity of the results to these parameters. The intensity of S controls the maximum ion courant that can be extracted since (continuity equation)

$$\Gamma_{ic} + \Gamma_{ia} = \int_0^d S(x)dx, \quad (5)$$

where Γ_{ic} and Γ_{ia} are the absolute values of the azimuthally averaged ion fluxes to the cathode and to the anode boundary. As said above and indicated in Fig. 3, the injected azimuthally averaged electron flux Γ_{ec} must satisfy
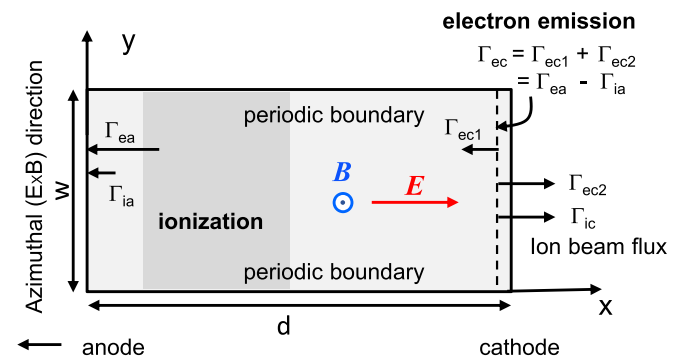
FIG. 3. Axial (x)–azimuthal (y) simulation domain. The azimuthal and axial dimensions, w and d, are 1 cm and 2.5 cm in most simulations presented here. Cathode emitted electrons are injected along the dashed line at the abscissa $x_c = 2.4$ cm (electron emission line). The darker zone is the ionization region. The value of the azimuthally averaged potential on the electron emission line is set to zero and the potential on the left boundary is V_a.

$$\Gamma_{ec} = \Gamma_{ea} - \Gamma_{ia}, \tag{6}$$

where Γ_{ea} and Γ_{ia} are the azimuthally averaged electron and ion fluxes to the anode side (absolute values). The electron flux out of the simulation domain on the cathode side Γ_{ec2} is equal to the ion flux, Γ_{ic}, through the same boundary (this is not imposed and must be a result from the simulation). Finally, the azimuthally averaged electron flux to the anode, Γ_a, and electron flux injected into the channel, Γ_{ec1}, must satisfy the relation

$$\Gamma_{ea} = \Gamma_{ec1} + \int_0^d S(x)dx. \tag{7}$$

Using Eqs. (1) and (3), the net electron flux (or current density) entering the channel from the cathode side, Γ_{ec1}, is obtained by measuring Γ_{ea}, Γ_{ia}, and Γ_{ic} in the simulation

$$\Gamma_{ec1} = \Gamma_{ea} - \Gamma_{ia} - \Gamma_{ic}. \tag{8}$$

The maximum ion current, J_M, that can be extracted from the channel is related to the ionization rate by

$$J_M = e(\Gamma_{ic} + \Gamma_{ia}) = e \int_0^d S(x)dx. \tag{9}$$

Practically, the injection of particles into the domain is performed as follows. Electrons are injected randomly at each time step along the cathode emission line (Fig. 3) and the number of electrons injected during a time interval δt (per unit length in the direction perpendicular to the simulation plane) is $\Gamma_{ec} w \delta t$, with Γ_{ec} being estimated from the measured value of $(\Gamma_{ea} - \Gamma_{ia})$ at the previous time step.

To simulate ionization, electron-ion pairs are injected at each time step according to the profile of the given ionization rate $S(x)$ (S is uniform in the azimuthal direction and is a function of x only). This means that the number of electron-ion pairs generated during each time interval δt per unit length in the direction perpendicular to the simulation plane is $w \delta t \int_0^d S(x)dx$, and the positions (x_i, y_i) are chosen randomly according to the S profile

$$r_1 = \frac{\int_0^{x_i} S(x)dx}{\int_0^d S(x)dx} \quad \text{and} \quad y_i = r_2 w, \tag{10}$$

where r_1 and r_2 are two random numbers uniformly distributed over the interval [0,1].

In the simulations shown here, the ionization rate has the cosine profile displayed in Fig. 4, given by

$$\left. \begin{aligned} S(x) &= S_0 \cos\left(\pi \frac{x - x_M}{x_2 - x_1}\right) \text{ for } x_1 \le x \le x_2, \quad \text{with } x_M = \frac{x_1 + x_2}{2} \\ S(x) &= 0 \quad \text{for } x < x_1 \quad \text{or } x > x_2 \end{aligned} \right\}. \tag{11}$$

Using this expression of $S(x)$, the abscissa x_i of a generated electron-ion pair in Eq. (10) can be easily obtained analytically. In all the simulations presented in this paper, the profile of the ionization rate $S(x)$ is given by Eq. (11) with fixed values of x_1 and x_2: $x_1 = 0.1, d = 0.25$ cm and $x_2 = 0.4, d = 1$ cm. A parametric study is performed by only changing the value of S_0 in Eq. (11). This is equivalent to changing the maximum ion current density J_M that can be extracted. J_M is directly proportional to S_0

$$J_M = e \int_0^d S(x)dx = \frac{2}{\pi}(x_2 - x_1)e S_0. \tag{12}$$

The chosen range of variations of S_0 in the simulations is such that J_M varies between 50 and 400 A/m². "Real" Hall thrusters operate (whatever their size) for current densities around 1000 A/m².[1,2] We chose lower values of the current density to speed up the calculations but we consider that 400 A/m² is sufficiently close to real values for the purpose of this simplified approach. The velocity distribution function of electrons injected from the cathode or generated by ionization is supposed to be Maxwellian and isotropic, with a temperature $T_e = 10$ eV. The velocity distribution of ions generated by ionization is also Maxwellian with a temperature $T_i = 0.5$ eV.

It is known that the contribution of electron-atom collisions to cross-field transport is not sufficient to explain electron conductivity in the region of large magnetic field.[2] Since we are mainly interested in the development of instabilities leading to anomalous electron transport, electron and ion collisions with neutral atoms as well as collisions
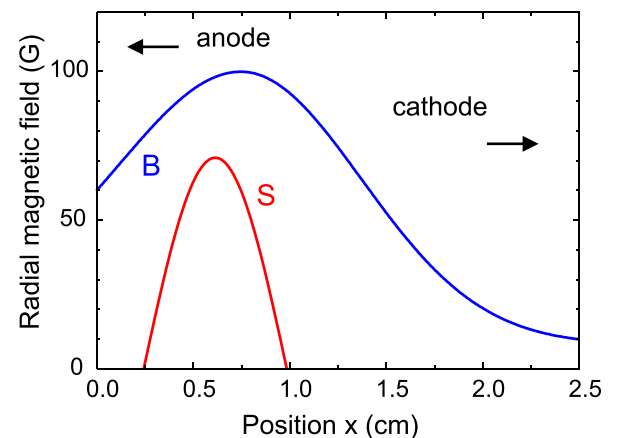

FIG. 4. Axial profiles of the radial magnetic field and of the ionization rate in the simulations (the anode region is not described).

between charged particles are neglected in the simulations presented here.

B. Magnetic field profile

The profile of the radial magnetic field is given by an analytical expression. The values of the magnetic field $B_0 = B(0)$, and $B_d = B(d)$, at $x = 0$ and $x = d$ as well as at the value at the maximum $B_{\max}$ at the abscissa $x_{B_{\max}}$ are given as parameters and the magnetic field profile is assumed to be Gaussian of the form

$$B(x) = a_k \exp\left(-\frac{(x - x_{B_{\max}})^2}{2\sigma_k^2}\right) + b_k \qquad (13)$$

with $k = 1$ for $x < x_{B_{\max}}$ and $k = 2$ for $x > x_{B_{\max}}$. a_1, b_1, a_2, b_2 can be easily calculated if $x_{B_{\max}}$, $B_{\max}$, B_0, B_d are given.

In the simulations presented here, the values of these parameters are (unless mentioned otherwise): $B_0 = 6\,\text{mT}$, $B_d = 1\,\text{mT}$, $B_{\max} = 10\,\text{mT}$, $x_{\max} = 0.3, d = 0.75\,\text{cm}$, and $\sigma_1 = \sigma_2 = 0.25, d = 0.625\,\text{cm}$.

The profile of the radial magnetic field is shown in Fig. 4.

C. Boundary conditions for the potential

The way cathode emitted electrons are injected into the simulation domain (see above) does not prevent an artificial sheath to form in front of the right boundary (because each electron reaching the right boundary of the simulation domain is lost). In order to fix the value of the plasma potential at the abscissa x_c of electron emission (emission line in Fig. 3), the potential is corrected at each time step by imposing a zero azimuthally averaged potential at this location. Doing this, the right boundary is at a negative potential that can vary in time (the drop in potential between the location of electron emission and the right boundary has no useful physical meaning), but the potential drop between the anode and the (azimuthally averaged) potential of the electron emission line is constant and equal to the applied voltage. The electric potential is obtained as follows:

$$\phi(x, y) = U(x, y) - x/x_c \bar{U}_c, \qquad (14)$$

where $\phi(x, y)$ is the electric potential at the location (x, y) and U is the solution of Poisson's equation

$$\Delta U = -\frac{e}{\varepsilon_0}(n_i - n_e), \qquad (15)$$

with boundary conditions $U(0, y) = V_a$; $U(d, y) = 0$, and with

$$\bar{U}_c = \frac{1}{w}\int_0^w U(x_c, y)dy. \qquad (16)$$

The electric potential ϕ therefore satisfies Poisson's equation, the azimuthally averaged value of ϕ at x_c is 0, and the azimuthally averaged potential difference between the cathode emission line and the "anode" is equal to the applied voltage V_a. The applied voltage V_a is set to 200 V in the

simulations presented in this paper. Note that the left boundary of the simulation domain is called "the anode" although the anode in a real Hall thruster would be located further away upstream. We are mainly interested here in electron and ion transport in the ionization and acceleration regions so we do not describe the full channel length (moreover, a shorter length of the simulation domain allows faster calculations).

D. PIC method, constraints, and accuracy

The PIC simulation is explicit (i.e., Poisson's equation is solved at the beginning of each time step and charged particles move during each time step assuming that the electric field does not change during that time step). This implies some strong constraints on the grid spacing δx and integration time step δt, which must satisfy[24] $\delta x < \lambda_{De}$ and $\delta t < 0.2/\omega_{pe}$ where λ_{De} and ω_{pe} are, respectively, the electron Debye length and angular plasma frequency. For the conditions above, with current densities below $400\,\text{A/m}^2$ we found that the Debye length was larger than $50\,\mu\text{m}$ and the plasma frequency was on the order or less than $3 \times 10^{10}\,\text{s}^{-1}$ so we used a spatial grid of 500×200 and a time step on the order of 0.5×10^{-11} s. Accuracy and convergence of the results were tested and verified by using two different Particle-In-Cell simulation codes and varying the grid size and the number of particles per cell (see Sec. V). The PIC simulation code noted Code 1 in the following was used for similar simulations presented in Ref. 19 and for simulations in other contexts.[25–28] The PIC simulation code indicated Code 2 was described and used in Refs. 29 and 30. The two codes have been developed independently but are based on the same core principles of explicit Particle-In-Cell simulations.[31] One difference is that Code 1 uses digital filtering[31] of the space charge before solving Poisson's equation, while Code 2 does not. Their implementation is slightly different since Code 1 is parallelized with the OpenMP (Open Multi-Processing) programming interface and operates on a 10 core processor, while Code 2 uses both OpenMP and MPI (Message Passing Interface) and operates on hundreds of cores.

IV. PIC SIMULATION OF THE $E \times B$ EDI

The PIC simulation results discussed in this section have been obtained, as said above, with given radial magnetic field and ionization rate profiles (shown in Fig. 4), and neglecting collisions between charged particle and neutral atoms (using the ion mass of xenon). The aim is to study the development of instabilities leading to anomalous cross-field electron transport, and to compare the scaling laws obtained with the PIC simulations with those of the $E \times B$ EDI theory.

Unless specified otherwise, the simulations reported in this section have been performed with code 2 and with a 500×200 grid and 280 particles per cell. The time step was such that $\delta t < 0.2\omega_{pe}^{-1}$ where ω_{pe} is the maximum electron plasma angular frequency. Similar simulation results have been published in Ref. 19 using code 1 with a similar grid spacing but with a smaller number of particles per cell.

The main parameter that is varied in the simulations presented here is the maximum total ion current density (production rate of electron and ion charges by ionization) J_M that can be extracted from the thruster. This parameter is changed by changing the value of S_0 in Equation (11) while keeping the same profile and the same values of x_1 and x_2.

The simulations are run for a time long enough to reach a steady state. Practically, the simulation time is several tens ion transit times in the channel, i.e., several tens of μs. The simulations are started with a uniform quasineutral plasma (initial density of 5×10^{16} m^{-3} in most cases, but the steady results are independent of the initial density). In most situations, we find that the $\boldsymbol{E} \times \boldsymbol{B}$ Electron Drift Instability forms in a short time after the acceleration region has formed and the ions have been accelerated.

A. Description of the instability

The instability is characterized by the development of an azimuthal wave with large amplitude oscillations of the azimuthal electric field and electron density as shown in Fig. 5 in the case $J_M = 400 \, \text{A/m}^2$. This figure shows the axial-azimuthal distributions of the azimuthal field and of the ion density at a given time during the wave propagation. Figure 6 shows the fluctuations of the ion density and azimuthal
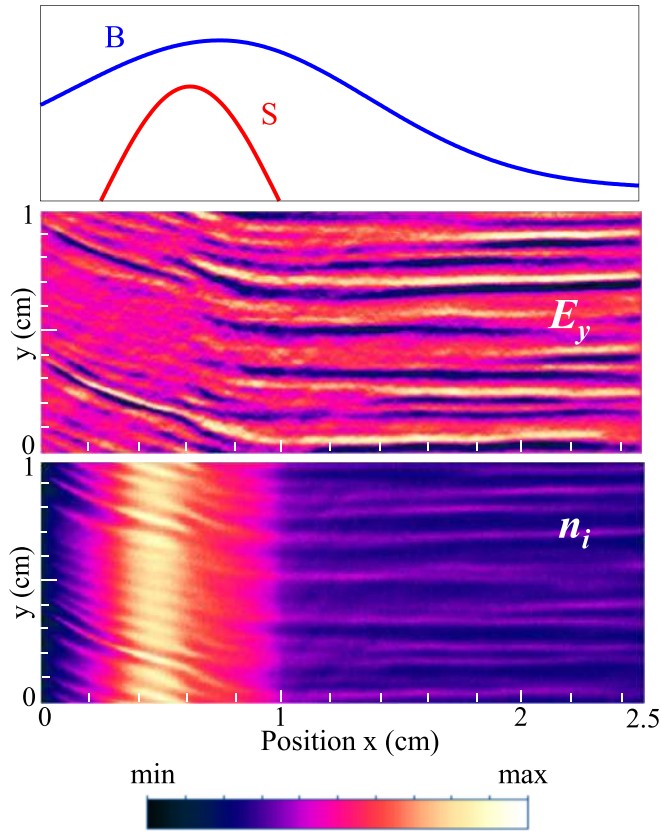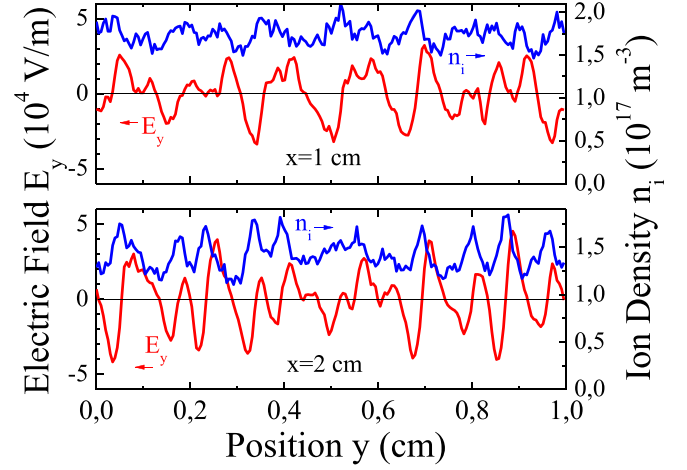
FIG. 6. Ion density and azimuthal fluctuations as a function of azimuthal position and at two axial positions, x = 1 cm, and x = 2 cm, in the conditions of Fig. 5.

electric field in the azimuthal direction at two axial positions. The time averaged electron density, accelerating (axial) electric field, and electron temperature are shown in Fig. 7.

The azimuthal wave appearing in the simulation exhibits in these conditions (Figs. 5 and 6) a dominant wavelength on the order of 800 μm in the conditions of Fig. 5. This is to be compared with a wavelength $\lambda_w \approx 2\pi\sqrt{2}\lambda_{De} \approx 9\lambda_{De}$ for the

FIG. 5. Axial-azimuthal distributions of the azimuthal electric field E_y and of the ion density n_i for a total production rate of electrons and ions by ionization equal tot $J_M = 400$ A/m^2. The axial distributions of the magnetic field and ionization rate are shown on top of the contour plots. The minimum and maximum values for E_y are -5×10^4 and $+5 \times 10^4$, respectively, and for n_i are 0 and 5×10^{17} m^{-3}. The applied voltage is 200 V. The wave propagates in the negative y direction ($\boldsymbol{E} \times \boldsymbol{B}$ direction).
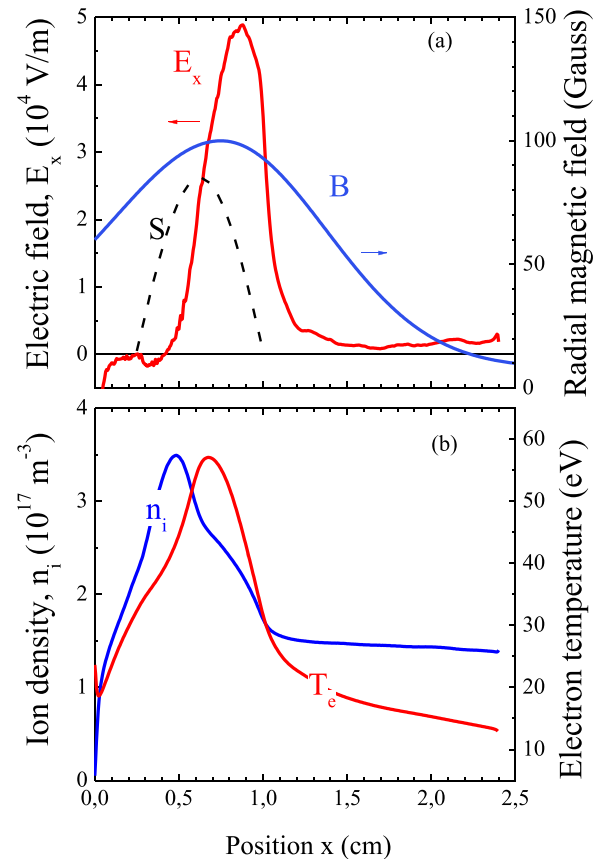
FIG. 7. (a) Time averaged and azimuthally averaged axial profiles of calculated axial electric field E_x and imposed radial magnetic field B and ionization rate S for $J_M = 400$ A/m^2 (conditions of Fig. 5); (b) Profiles of the ion density and electron temperature under the same conditions.

modified ion acoustic instability at the maximum growth rate. The electron Debye length is between $80\,\mu m$ and $110\,\mu m$ in the acceleration region so the theoretical wavelength should be between $700\,\mu m$ and $1\,mm$, i.e., on the order of the wavelength observed in the simulation.

The phase velocity of the wave in the $\boldsymbol{E}\times\boldsymbol{B}$ direction can be deduced from the simulation and is on the order of $5\times10^3\,m/s$. According to the theory of the modified ion acoustic instability (Sec. II), the phase velocity of the wave is $v_w = \omega_{max}/k_{max} \approx c_s\sqrt{2/3}$. In our conditions, the maximum electron temperature is $60\,eV$ (Fig. 7) so the ion acoustic velocity $c_s = \sqrt{T_e/M}$ is on the order of $6\times10^3\,m/s$ and $c_s\sqrt{2/3}$ is therefore about $5\times10^3\,m/s$, similar to the wave velocity deduced from the simulation.

The wave angular frequency $\omega = k_{max}v_w = v_w/\left(\sqrt{2}\lambda_{De}\right)$ is therefore on the order of $5\times10^7\,rd/s$ and is also close to the value corresponding to the modified ion acoustic instability, $\omega_{max} \approx \omega_{pi}/\sqrt{3}$. The maximum of the time averaged accelerating electric field shown in (Fig. 7) is about $5\times10^4\,V/m$ and is located close to the maximum magnetic field. The overlap between the ionization region and the acceleration region is important in these conditions. As mentioned above, the maximum electron "temperature" is $60\,eV$ [Figs. 7(b) and 8].

The maximum mean electron kinetic energy is about $110\,eV$ [electron thermal energy of $90\,eV$ plus about $20\,eV$ of directed azimuthal energy, see Fig. 8(a)]. Since

electron-neutral collisions are not taken into account, there are no energy losses due to collisions, and the fact that the electron mean energy does not simply increase with electric potential is due to the injection of low energy electrons which leads to a decrease in the electron mean energy in the ionization region. Note that the electron temperature is not isotropic [Fig. 8(b)].

Since there is no scattering due to collisions and the simulations are 2D in the (x,y) plane, the temperature in the z direction is constant and equal to the temperature ($10\,eV$) of injected electrons along the cathode line or by ionization. Heating by the wave is clearly apparent through the large value of the azimuthal electron temperature. The difference between the calculated azimuthal drift energy $1/2mu_y^2$ and $1/2m(E/B)^2$ seen in Fig. 8(a) is due to the large contribution of the pressure gradient term $\partial_x(n_e T_{ex})/B$ (diamagnetic term) to the azimuthal drift velocity, as can be seen in Fig. 8(c).

The axial pressure gradient term $\partial_x(n_e T_{ex})$ is smaller but on the same order (and in the opposite direction) as the electric field term E_x in the acceleration region, leading to a significant reduction of the azimuthal drift velocity in the acceleration region. The still large value of u_y and $1/2mu_y^2$ upstream of the acceleration region is mainly due to the diamagnetic contribution to the azimuthal electron drift since the axial electric field is very small in this region.

The axial variations of the rms azimuthal fluctuations of the azimuthal electric field, electric potential, and ion density are shown in Fig. 9. The rms fluctuations as a function of the axial position of a given quantity $A(x,y,t)$, noted $\delta A_{rms}(x)$ below, are defined as

$$\delta A_{rms}(x) = \frac{1}{N}\sum_{k=1}^{N}\left[\int_0^w A^2(x,y,t_k)\frac{dy}{w} - \left(\int_0^w A(x,y,t_k)\frac{dy}{w}\right)^2\right]^{1/2},$$

(17)

where the average in time is made over typically $N=100$ instants uniformly distributed over $5\,\mu s$ after convergence of the simulation.

We see in Fig. 9 that the azimuthal field fluctuations are very large since the rms values of these fluctuations are on the same order as the axial accelerating electric field (several
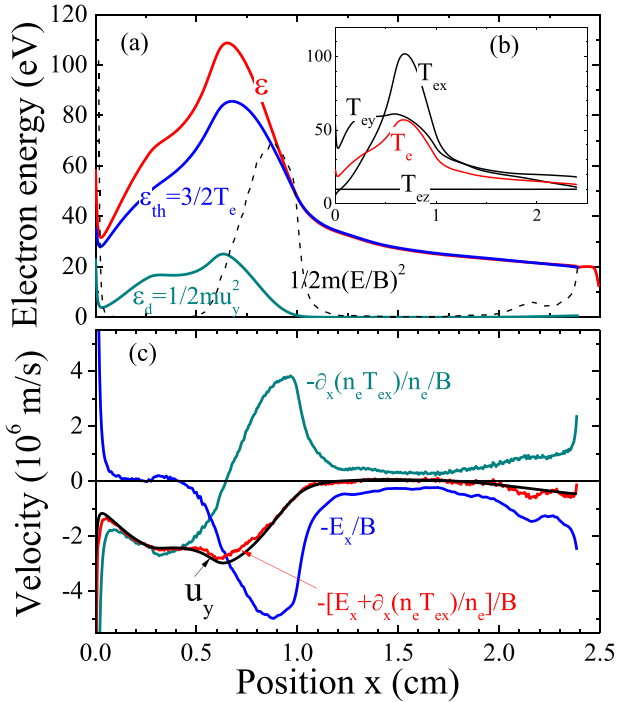

FIG. 8. (a) Time and azimuthally averaged total electron mean kinetic energy, electron thermal energy, and azimuthal drift energy as a function of axial position in the conditions of Fig. 5. u_y is the calculated azimuthal drift velocity (different from E/B because of the contribution of diamagnetic drift); $1/2m(E/B)^2$ is also shown (dashed line) for comparison with $1/2mu_y^2$; (b) axial distribution of electron temperature and electron temperatures in the three directions; (c) calculated azimuthal drift velocity u_y as a function of axial position, and contributions of the axial field and axial pressure gradient terms to u_y.
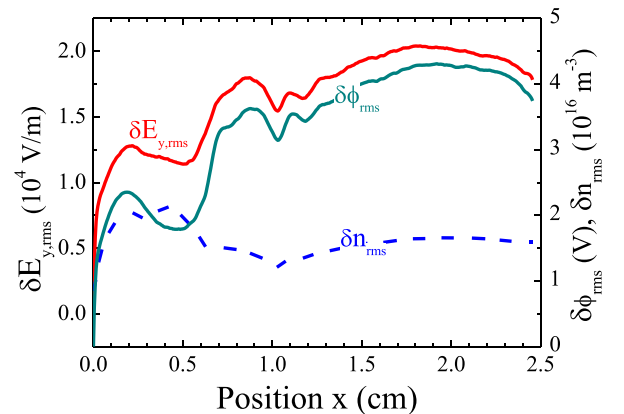

FIG. 9. Axial variations of the rms azimuthal fluctuations of the azimuthal electric field, ion density, and electric potential, in the conditions of Fig. 7.

10^4 V/m). The potential fluctuations are of course consistent with the value of the wavenumber and wavelength of the azimuthal wave: $\delta\phi_{rms} \approx \delta E_{y,rms}/k_{max} = \delta E_{y,rms}\lambda_w/(2\pi)$. The rms plasma density fluctuations are between 5% and 10% of the plasma density. It is interesting to note that the fluctuations are large not only in the acceleration region, i.e., between x = 0.5 cm and x = 1.2 cm [see Fig. 7(a)], where the instability is driven by the large $\boldsymbol{E} \times \boldsymbol{B}$ drift, but also in the region downstream of the acceleration region where the axial field is very small. This indicates that the instability, i.e., the azimuthal non uniformity of the plasma, is convected by the axial ion flow (this is clearly seen in the azimuthal field and density plots of Figs. 5 and of 11 below). The reason for the slight increase in the rms values of the potential and azimuthal field fluctuations downstream of the acceleration region (Fig. 9), where the instability is no longer excited, is not clearly understood.

B. Saturation of the instability

The theory based on the assumption that saturation of the ion acoustic wave is due to ion-wave trapping (see Sec. II above) predicts rms azimuthal field and electric potential oscillations of the form $\delta E_{y,rms} = T_e/(12\lambda_{De})$ and $\delta\phi_{rms} = T_e/(6\sqrt{2})$.

The plasma density fluctuations can be approximated as

$$\delta n_{rms}/n \approx \delta\phi_{rms}/T_e = \left(6\sqrt{2}\right)^{-1}. \tag{18}$$

We can estimate values of the above theoretical expressions of the rms fluctuations of the electric field, electric potential, and plasma density, based on the assumption of ion wave trapping saturation, and compare them to those obtained in the simulations and shown in Fig. 9. For example, at the abscissa $x = 1$ cm at the end of the acceleration region (where $n \approx 1.7 \times 10^{17}\,\text{m}^{-3}$ and $T_e \approx 30\,\text{eV}$, see Fig. 7) the theory gives $(\delta E_{y,rms})_{th} \approx 2.6 \times 10^4\,\text{V/m}$, $(\delta\phi_{rms})_{th} \approx 3.7\,\text{V}$, and $(\delta n_{rms}/n)_{th} \approx 0.12$(constant according to the theory). From the PIC simulations, these quantities are (see Fig. 9) $(\delta E_{y,rms})_{PIC} \approx 1.6 \times 10^4\,\text{V/m}$, $(\delta\phi_{rms})_{PIC} \approx 3.3\,\text{V}$, and $(\delta n_{rms}/n)_{PIC} \approx 0.07$. The amplitudes of the fluctuations in the simulations are smaller than those corresponding to ion wave trapping but considering that the theoretical values are rough estimations, we can say that ion wave trapping is a plausible mechanism of saturation of the instability (more detailed comparisons are described in the parametric study below).

Information on ion wave trapping can also be obtained from the ion velocity distribution in the azimuthal direction. Figure 10(a) shows the y-v_y phase plot of ions located between x = 1.75 cm and x = 2 cm, i.e., downstream of the acceleration region. This figure exhibits the presence of trapped ions with maximum azimuthal velocity close to $\omega_{max}/k_{max} + v_{trap}$ (on the order of $6 - 7 \times 10^3$ m/s in these conditions) with $v_{trap} = 2\sqrt{e/M\delta\tilde{\phi}}$, i.e., satisfying the trapping conditions discussed in Ref. 18 and in Sec. II above. The ion azimuthal velocity distribution integrated along the azimuthal direction y is plotted in Fig. 10(b), at three different axial locations and exhibits a tail with maximum velocities around $\omega_{max}/k_{max} + v_{trap}$. It also appears in Fig. 10(b)
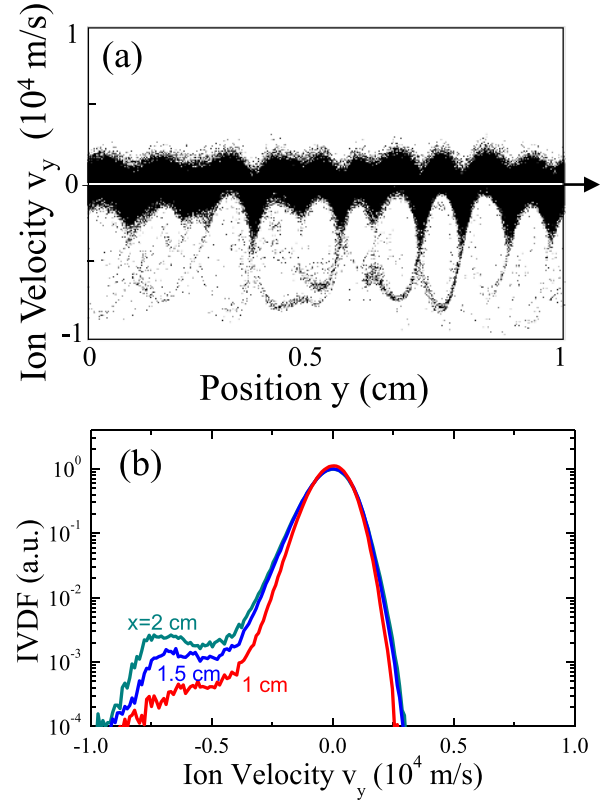

FIG. 10. (a) y-v_y phase space of the ions with axial positions between x = 1.75 cm and x = 2 cm in the conditions of Fig. 5; (b) Ion velocity distribution function (azimuthally integrated) at three axial positions under the same conditions.

that ions continue to gain azimuthal energy from the convected wave, downstream of the acceleration region.

We conclude that for the conditions considered in this section ($J_M = 400\,\text{A/m}^2$), the predictions of the PIC simulations concerning wavelength and frequency of the instability are consistent with the numbers corresponding to an azimuthal ion acoustic wave, and that the mechanism of saturation of the instability is consistent with ion wave trapping . We study below the scaling of the instability with J_M, i.e., with the plasma density.

C. Parametric study and scaling of the instability

We have seen above that, for $J_M = 400\,\text{A/m}^2$, the main characteristics of the wave, wavelength, phase velocity, and frequency are in relatively good agreement with the numbers corresponding to the modified ion acoustic instability.

According to the scaling of the modified ion acoustic instability theory, we expect the wavelength (proportional to the Debye length) to increase with decreasing J_M (i.e., with decreasing plasma density). In this section, we perform a parametric study by varying the maximum ion current J_M between 50 A/m^2 and 400 A/m^2 .

Figure 11 shows the axial-azimuthal distributions of the azimuthal electric field and ion density for $J_M = 50, 100, 200,$ and 400 A/m^2. We see in this figure that the wavelength of the fluctuations increases with decreasing J_M (i.e., with decreasing plasma density) and that the amplitude of the azimuthal field and plasma density fluctuations decrease with

E_y n_i

J_M=400 A/m²

200 A/m²

100 A/m²©

50 A/m²

y (cm)

Position x (cm)   Position x (cm)

min ▬▬▬ max

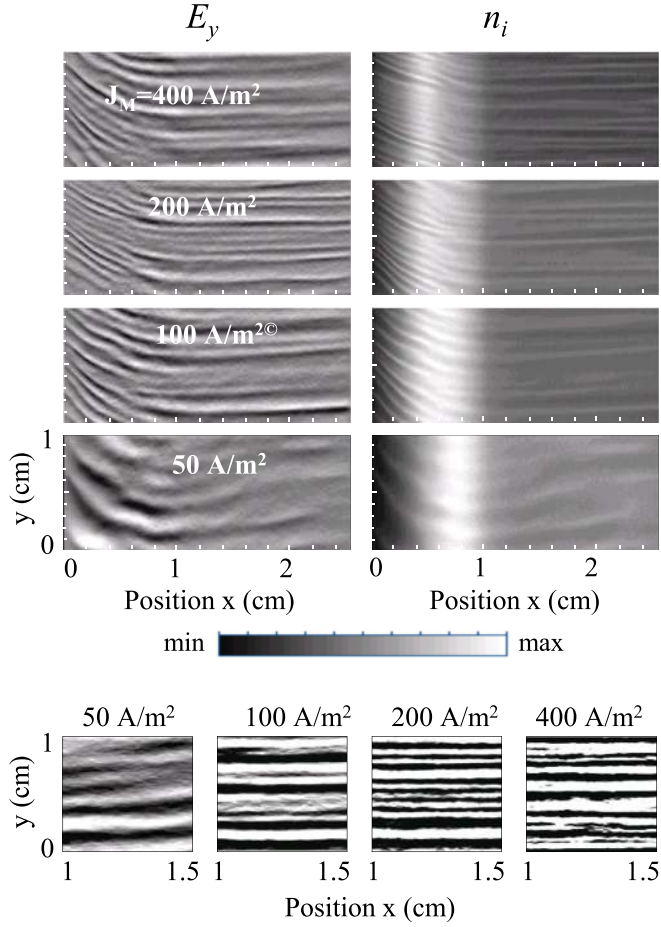50 A/m²   100 A/m²   200 A/m²   400 A/m²

Position x (cm)

FIG. 11. (top) Distributions of the azimuthal electric field and ion density at a given time (after convergence of the simulation) for four different values of the maximum ion current J_M: 50, 100, 200, and 400 A/m². The applied voltage is 200 V. The min-max values are ± 1.1, ± 1.5, ± 3.5, $\pm 5.5 \times 10^4$ V/m, for the azimuthal field and the ion density is plotted between 0 and 4×10^{16} m⁻³, 10^{17} m⁻³, 2×10^{17} m⁻³, and 4×10^{17} m⁻³, for 50, 100, 200, 400 A/m², respectively; (bottom) distribution of the azimuthal electric field between $x = 1$ cm and $x = 1.5$ cm for the four values of the current density J_M and plotted with a scale (-3000 V/m, $+3000$ V/m) allowing a rough estimate of the instability wavelength.

decreasing J_M. The scaling of these quantities with J_M and with the plasma parameters is described below and compared with the theory. Another interesting feature of Fig. 11 is that the axial wavenumber, which is close to zero at 400 A/m², increases when the ion current density decreases. We will comment on this feature at the end of this section.

Figure 12 shows comparisons between the PIC simulations and the theory. Figure 12(a) displays the wavelength at the position x = 1 cm and wave phase velocity as a function of the total ion current J_M, deduced from the PIC simulations and compared with the theory of the modified ion acoustic instability. The dominant wavelength is roughly estimated by counting the number of maxima of the electric field above a given value around the end of the acceleration region (see the bottom of Fig. 11) or by counting the number of loops in the y-v$_y$ ion phase space [Fig. 10(a)]. A more systematic Fourier analysis is left for future work. The agreement between simulation and theory is relatively good, showing that the simulations roughly follow the scaling $\lambda_w \approx 2\pi\sqrt{2}\lambda_{De}$ and $v_w \approx c_s\sqrt{2/3}$, and therefore $\omega_w \approx \omega_{pi}/\sqrt{3}$. The rms values of the electric field,
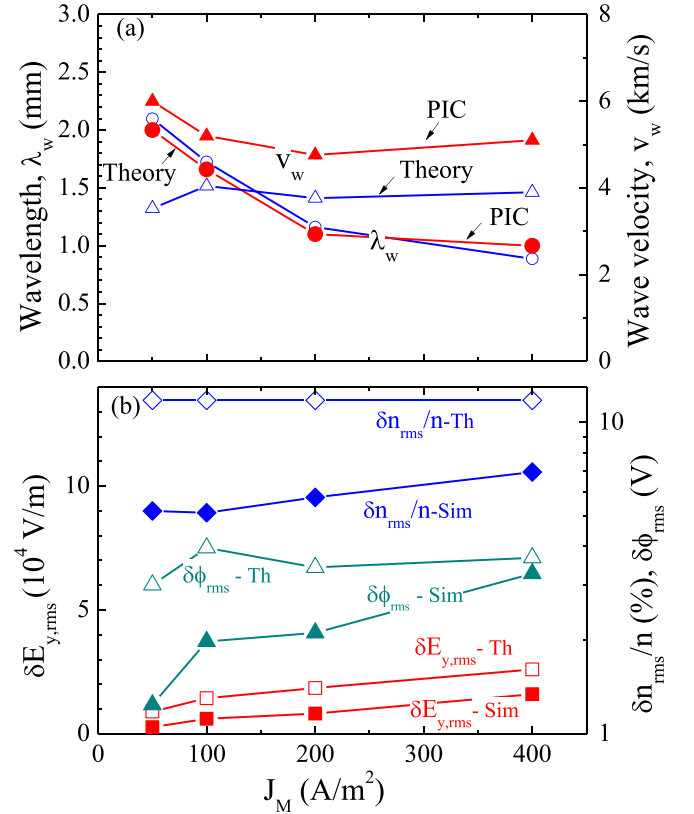

FIG. 12. (a) Wavelength λ_w(circles) and phase velocity v_w (triangles) at the location $x = 1$ cm at the end of the acceleration region deduced from the PIC simulations (full symbols), as a function of total ion current J_M, compared with the theory (open symbols) of the modified ion acoustic instability, $\lambda_w \approx 2\pi\sqrt{2}\lambda_{De}$, and $v_w \approx c_s\sqrt{2/3}$ (calculated for the plasma density and electron temperature at the same location as in the PIC simulations; (b) Comparison between the rms electric field, electric potential, and relative ion density fluctuations obtained from the PIC simulations at the location of maximum magnetic field, with those predicted by the theory of modified ion acoustic instability assuming saturation by ion wave trapping (results from code 2 with the same grid and 280 particles per cell).

electric potential, and relative ion density fluctuations, as a function of total ion current density J_M, are shown in Fig. 12(b) and compared with the estimations (Sec. II) of the values corresponding to saturation by ion wave trapping. The theoretical estimations of fluctuations associated with saturation by ion wave trapping give larger values than those observed in the particle simulations. This difference is not really significant because of the very rough theoretical estimations. In the larger current density case $J_M = 400$ A/m², we have seen above (Fig. 10) that the phase space plot and ion velocity distribution functions exhibit features that are characteristic of particle wave trapping. This is less true for the lower current density case where the phase space loops and high energy tail of the ion distribution seen in Fig. 10 are much less pronounced. In this case, the azimuthal field fluctuations are smaller and the ions are convected out of the acceleration region before they can be efficiently accelerated by the wave field in the azimuthal direction.

D. Current densities and effective Hall parameter

From the results and discussion above, it appears that the amplitude of the field fluctuations decreases with decreasing J_M and decreasing plasma density.

We therefore expect that the anomalous electron transport, or the effective electron mobility, will also decrease with decreasing plasma density. An interesting way to look at this is to plot the different current densities flowing in and out the channel. For example, the electron current density J_{ec1} entering the channel adjusts itself to neutralize the extracted ion beam. Since the beam ion density is fixed by the ion current density and applied voltage, J_{ec1} is directly related to the effective cross-field electron transport and mobility and its value or, more precisely, the J_{ec1}/J_M ratio is a measure of the anomalous cross-field transport.

Figure 13 shows the variations of J_{ec1}/J_M and J_{ic}/J_M as a function of the imposed maximum ion current density J_M in the conditions of Fig. 11. We see that J_{ec1}/J_M increases quasi-linearly with J_M, which means that the effective electron mobility in the region where the instability is convected increases in the same way with the plasma density.

The J_{ic}/J_M ratio slightly decreases with J_M and is close to 1, meaning that practically all the ions generated in the ionization region are extracted on the cathode side under these conditions. A small fraction reaches the anode (this fraction increases with increasing J_M). The value of J_{ec1}/J_M for $J_M = 400\,\mathrm{A/m^2}$ is quite large; the electron current entering the channel is larger than the extracted ion current. This is not typical of satisfactory operation of a Hall thruster where the electron current entering the channel is expected to be a fraction of the extracted ion current (on the order or less than 30%). This is because the conditions of the simulations are not those of a real Hall thruster (smaller magnetic field, imposed position and profile of the ionization source, etc.). Nevertheless, the simulation results indicate a clear influence of the plasma density on the electron anomalous mobility and this is correlated with the amplitude of the azimuthal field fluctuations.

The anomalous electron transport can also be characterized by an effective Hall parameter or effective collision frequency. The Hall parameter is defined as the ratio $h = \Omega_{ce}/\nu$, where ν is the averaged electron collision frequency. In the collisionless conditions considered in this paper, ν is an effective collision frequency associated with anomalous cross-field electron transport. The electron mean velocity components in the axial and azimuthal directions can be written, respectively, as (E_x^* includes the pressure gradient term, see Fig. 8)

$$u_x = \frac{e}{m}\frac{\nu}{\Omega_{ce}^2}E_x^*; \quad u_y = \frac{E_x^*}{B}. \tag{19}$$

Therefore, the Hall parameter is equal to the ratio of the azimuthal to the axial electron mean velocity components and can be deduced from the PIC simulations by calculating this ratio. The effective Hall parameter, effective collision frequency, and anomalous cross-field electron mobility $\mu_{e,x} = \frac{1}{hB}$ at the location of maximum magnetic field are shown in Table I.

The simulations show that the effective electron mobility and effective collision frequency have a minimum around the maximum radial magnetic field. This is consistent with the self-consistent PIC MCC simulations of Adam et al.[5] Effective collision frequencies, Hall parameters, or electron cross-field mobilities in Hall thrusters have also been deduced from experiments[32,33] or have been adjusted to match experiments and models (see, e.g., Refs. 22 and 34). In many cases, the estimated effective collision frequency at the minimum around the maximum radial magnetic field is in the range $[2$–$6 \times 10^6\,\mathrm{s}^{-1}]$ which is consistent with the results of Table I. The results of Table I suggest that these effective collision parameters should also depend on the total ion current, i.e., on the xenon mass flow rate. The effective collision frequency and electron mobility increase by a factor of 4 when J_M increases form $50\,\mathrm{A/m^2}$ to $400\,\mathrm{A/m^2}$. To our knowledge, this has not been shown in experiments and it would be useful to experimentally investigate the dependence of the effective collision frequency in the exhaust region, on the mass flow rate.

Finally, we note that for low values of J_M (below 100 A/m²) the plasma density and current densities are not steady and present low frequency oscillations of several hundreds of kHz that modify the velocity distribution of the extracted ions, as shown in Fig. 14 and described below.

E. Ion beam energy distributions and transit time oscillations

When the total ion current density is decreased below $100\,\mathrm{A/m^2}$, anomalous electron transport is reduced and the
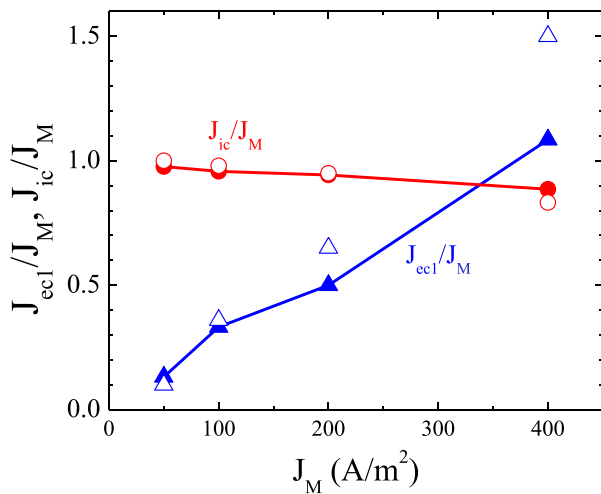

FIG. 13. Variations of the ratios of electron current density entering the channel and extracted ion current density on the cathode side to the maximum ion current density (imposed by the given ionization rate) in the conditions of Fig. 11. The full symbols correspond to the simulations using code 2 with a 500×200 grid and 280 particles per cell; the open symbols correspond to code 1 with the same grid and 40 particles per cell.

TABLE I. Hall parameter, effective electron collision frequency, and electron cross-field mobility calculated at the location of maximum magnetic field for different values of the total ion current J_M.

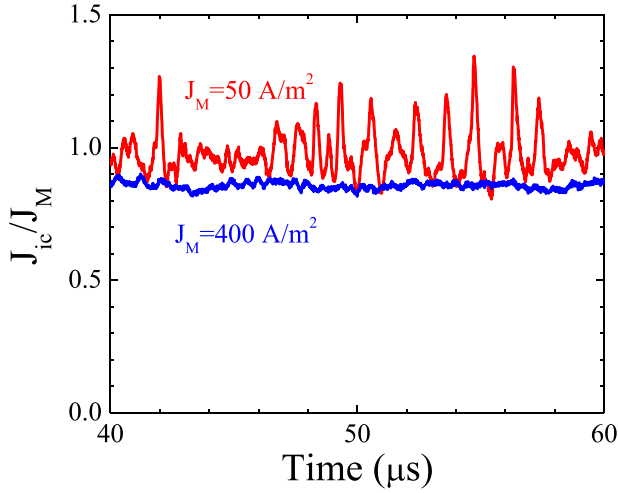|	h	ν_{eff} ($10^6\,\mathrm{s}^{-1}$)	$\mu_{ex,eff}$ (m²/V/s)
$J_M = 50\,\mathrm{A/m^2}$	770	2.1	0.13
$100\,\mathrm{A/m^2}$	500	3.2	0.2
$200\,\mathrm{A/m^2}$	370	4.3	0.27
$400\,\mathrm{A/m^2}$	192	8.3	0.52

FIG. 14. Time variations of the extracted ion current on the cathode side, normalized to J_M, for two values of J_M, obtained with code 1, 40 particles per cell.

FIG. 15. (a) and (b) Ion distribution functions F(x, ε) at a given time (log scale, 3 decades) for $J_M = 50\,\mathrm{A/m^2}$ and $J_M = 400\,\mathrm{A/m^2}$, respectively; (c) ion energy distribution at the position x = 2 cm for 50 A/m^2 and 400 A/m^2, respectively. Full black lines correspond to the instantaneous distributions of (a) and (b). Lines with symbols correspond to time averaged ion distributions. The ion distributions are integrated azimuthally (same normalization for all curves); (d) time averaged electric potential and axial electric field for the two cases. Open circle symbols: $J_M = 400\,\mathrm{A/m^2}$; full square symbols: $J_M = 50\,\mathrm{A/m^2}$. Obtained with code 1, 40 particles per cell.

electron conductivity induced by the purely azimuthal wave is no longer sufficient to provide the electron current necessary to neutralize the extracted ion flow downstream of the acceleration region. The consequence is the development of axial oscillations of the plasma and electric field, which can have a strong impact on the velocity distribution of the extracted ions.

These oscillations seem to be related to the so-called transit time oscillations[35–37] or resistive instabilities[38] (see Ref. 2 and references therein) which have been observed in some experiments and are present in hybrid models when the empirical anomalous transport parameters are too low,[39] e.g., when the electron conductivity is too low.

In the present model, these oscillations are associated with the increase in the axial wave number with decreasing J_M, as can be seen in Fig. 11. The axial oscillations are important in the simulations in the case $J_M = 50\,\mathrm{A/m^2}$. The perturbation propagates at the ion beam velocity (i.e., on the order of 15 km/s in our conditions) on a 1.5 cm length between the acceleration region and the cathode line. This corresponds to a frequency on the order of 1 MHz, related to the transit time of the ions between the acceleration region and the cathode line. Figure 14 shows the time variations of the normalized ion current extracted on the cathode side for two values of J_M, 50 A/m^2 and 400 A/m^2. Relatively large amplitude oscillations in the MHz range can be seen in the lower current case. In the 400 A/m^2 case, the ion current is practically not modulated in time.

As expected, the ion energy distribution function (Fig. 15) is affected by the axial oscillations. In the 400 A/m^2 case, the ion energy distribution function is clearly peaked around 240 V, while the distribution is much less beam-like in the 50 A/m^2 case. The simulations also show that the azimuthally averaged 400 A/m^2 ion distribution function is practically not modulated in time (the instantaneous and time averaged distributions are practically identical for 400 A/m^2 in [Fig. 15(c)] while the 50 A/m^2 distribution presents strong oscillations, as can be seen in Fig. 15(a) and in the difference in the instantaneous and time averaged distributions for 50 A/m^2 in Fig. 15(c).
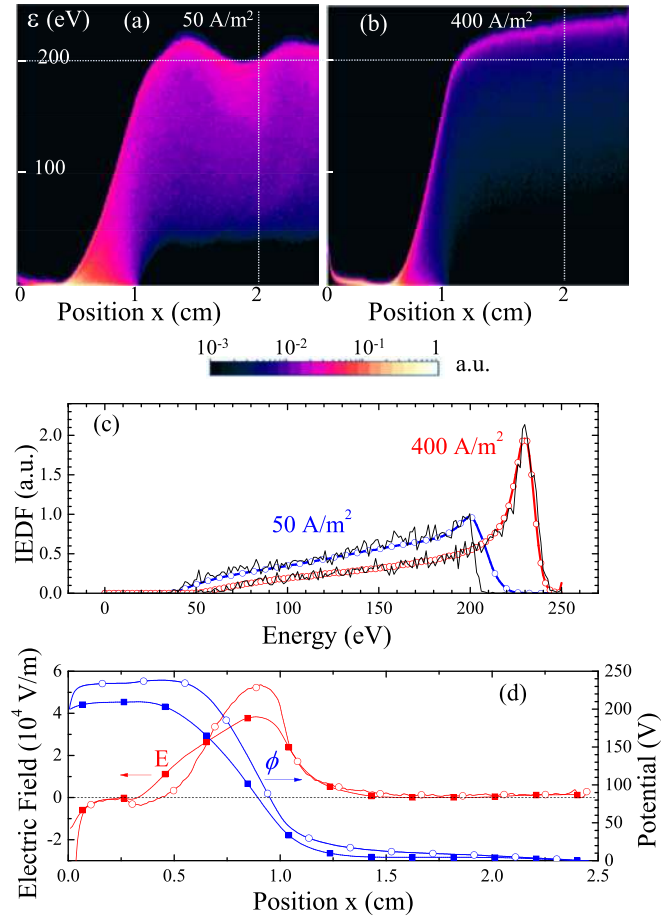
The beam energy in the 400 A/m^2 case is larger than the applied voltage 200 V, because the plasma potential in that case is 240 V, as can be seen in Fig. 15(d) (because of the large electron temperature and large electron conductivity).

In the 50 A/m^2 case, the plasma potential is on the order of 210 V (because of the lower electron conductivity) but some ions can have energy slightly larger than 210 eV [see Fig. 15(a) and the time averaged distribution in Fig. 15(c)] because of the oscillations in time of the axial electric field and ion distribution function ("wave-riding" ions). The ion energy distribution is much more spread out in the 50 A/m^2 case because of the axial field oscillations and of the larger overlap between the acceleration and ionization regions [the large axial field region extends deeper in the channel in the 50 A/m^2 case, as can be seen in Fig. 15(d)].

V. ACCURACY AND CONVERGENCE OF THE RESULTS

PIC simulations are subject to numerical noise leading to numerical diffusion and it is essential to check the

accuracy and convergence of the results, especially when anomalous electron transport is being investigated.

In this paper, we check the validity and convergence of the simulations 1) by comparing the results obtained by two different and separately developed codes (noted Code 1 and Code 2 in the following, see the end of Sec. III for references), 2) by performing simulations with different grid sizes and number of particles per cell, and 3) by comparing results with two different values of the width w of the simulation domain in the $E \times B$ direction (to check the effect of the assumed azimuthal periodicity on the results).

Figure 16(a) shows the ratio J_{ec1}/J_M of electron current entering the channel to the total ion current, as a function of the total ion current density for $w = 1$ cm and for a 500×200 mesh (i.e., grid spacing of $50 \, \mu$m), for different values of the number of particles per cell and for the two codes. Figure 16(a) is similar to Fig. 13, with the number of particles per cell as a parameter and without the plot of the ratio of extracted ion current on the cathode side to the total ion current (this ratio is actually not very sensitive to the number of particles per cell). We see that 18 particles per cell lead to a large overestimation of J_{ec1}/J_M, i.e., to an

overestimation of anomalous cross-field transport because of numerical noise. The variations of J_{ec1}/J_M with the number of particles per cell in the simulation are displayed in Fig. 16(b) for $J_M = 200 \, \text{A/m}^2$. The results for a 250×100 mesh (sufficient to resolve the Debye length at $200 \, \text{A/m}^2$) show that the error is still not negligible when the number of particles per cell is 280. The results seem to converge for a number of particles per cell above 1000 [Fig. 16(b)] in the $200 \, \text{A/m}^2$ case with a 250×100 mesh.

Note also that the results of simulations performed with only 40 particles per cell (and smoothing of the space charge before solving Poisson's equation) tend to overestimate anomalous transport but provide reasonable estimates of the electron current [Fig. 16(a)] or plasma fluctuations [Fig. 12(b)], compared with those obtained with 280 particles per cell (and no smoothing).

The case with a simulation domain with a larger azimuthal length (w = 4 cm) gives very similar results in terms of wavelength and wave frequency. The ratio J_{ec1}/J_M is also consistent with the results obtained for w = 1 cm, but more simulations need to be done to confirm convergence for a larger number of particles per cell and for large values of w.

VI. SUMMARY AND CONCLUSION

A simplified model based on Particle-In-Cell simulations has been used to study anomalous transport in a Hall thruster. The model is two-dimensional and includes the axial direction and a section of the azimuthal direction (assuming periodic boundary conditions) of a Hall thruster. Due to the large $E \times B$ electron drift, instabilities are likely to develop in the azimuthal, $E \times B$ direction and it is essential to describe this direction when studying anomalous transport. The physical model has been simplified by neglecting collisions, and using a given, non self-consistent ionization rate. This allows elimination of the complexity associated with the ionization instability and subsequent low frequency oscillations, in order to focus on the azimuthal instability.

The results of the PIC simulations confirm the formation of an instability in the $E \times B$, azimuthal direction, with wavelength in the mm range and frequency on the order of the ion plasma frequency. This instability has been previously evidenced by Adam et al.[4,5] in the context of Hall thrusters and is similar to the electron cyclotron drift instability that has been studied in the conditions of collisionless shocks in space plasmas. The instability is due to the large $E \times B$ electron drift in the azimuthal direction, more precisely to the large difference between electron and ion drift velocities in the azimuthal direction, the ions being practically not magnetized in these conditions. For this reason, following Cavalier et al.,[6] we call this instability $E \times B$ electron drift instability ($E \times B$ EDI). Using collective laser scattering measurements of the plasma density fluctuations in Hall thrusters, Tsikata et al.[8] have shown the presence of instabilities with wavelength and frequency consistent with the predictions of the particle simulations but with smaller amplitudes. Systematic measurements of this type in a large
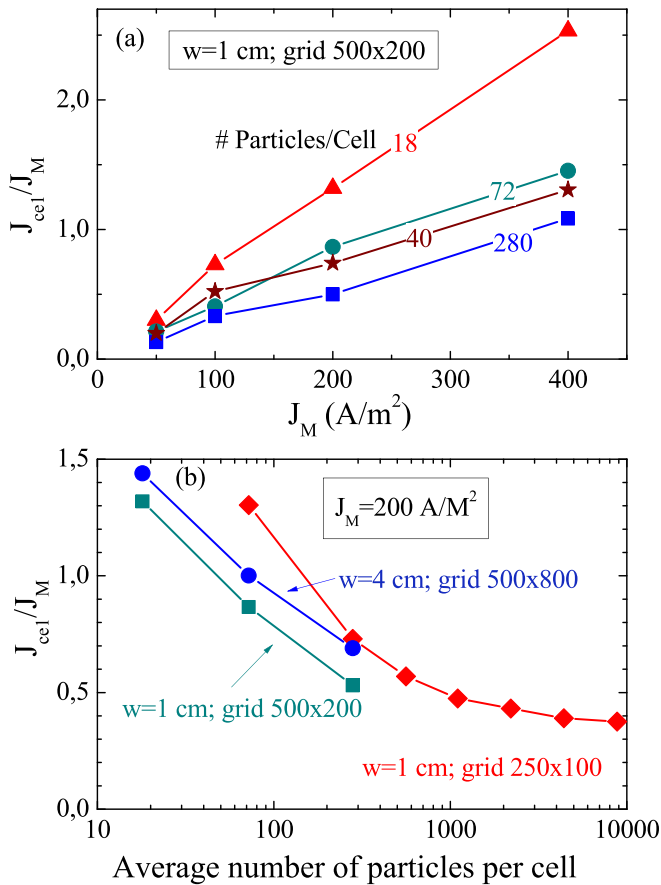

FIG. 16. (a) Ratio J_{ec1}/J_M, of the electron current entering the channel, to the total ion current as a function of the total ion current density J_M for different values of the average number particles per cell and for the two different codes (the star symbols correspond to code 1 and the other symbols to code 2); the width of the simulation domain in the azimuthal direction w is 1 cm, and the number of cells in the simulation is 500×200; (b) J_{ec1}/J_M as a function of the average number of particles per cell for $J_M = 200 \, \text{A/m}^2$, for two different grid spacings and for two values of w, $w = 1$ cm and $w = 4$ cm (code 2).

range of operating conditions would be extremely valuable for validation of the model predictions.

The $E \times B$ EDI forms in the acceleration region (where the electron drift velocity is large) and is convected downstream. The instability allows ("anomalous") electron transport across the magnetic field in the absence of collisions. The $E \times B$ EDI has a very large growth rate in the conditions of Hall thrusters and its presence is ubiquitous in PIC simulations where the azimuthal direction is described.

According to the theory, the $E \times B$ EDI results from electron Bernstein waves Doppler shifted towards low frequencies by the large electron drift velocity and merging into an ion-acoustic wave in the limit of a small Electron Debye length to Larmor radius ratio and a small $E \times B$ drift to electron thermal velocity ratio. The maximum growth rate of the instability occurs at a wavelength about ten times the electron Debye length ($\lambda = 2\pi\sqrt{2}\lambda_{De}$), which is on the order of 1 mm in the conditions of Hall thrusters. The phase velocity at the maximum growth rate of the wave in the azimuthal direction is close to the ion acoustic velocity and the angular frequency and growth rate are proportional to the ion plasma frequency.

The aim of the PIC simulations presented in this paper was to perform a parametric study of the instability observed in the simulations and to compare the scaling of the simulated instability with that of the modified ion acoustic instability. The parameter of the simulations is the total ion current density J_M produced by the given ionization rate (the axial profile of the ionization source term is fixed and its intensity can be varied). The variations with plasma density (defined by J_M) of the dominant wavelength and phase velocity of the simulated instability are consistent with those of the ion-acoustic instability. The rms fluctuations of the azimuthal electric field, electric potential, and relative ion density are smaller than simple and crude estimations of these fluctuations for saturation by ion wave trapping but the qualitative behavior of the wave-particle interaction is consistent with this mechanism of saturation for sufficiently large plasma densities.

The effective collision frequency (several 10^6 s^{-1}), Hall parameter, or electron mobility that can be deduced from the simulations in the region of maximum magnetic field are consistent with the values deduced from measurements, or with the values that must be used in hybrid models to reproduce experimental results.

An important aspect of these results is the dependence of the anomalous conductivity on the total extracted ion current (i.e., on the mass flow rate, or on the plasma density), everything else being kept constant. The effective collision frequency and electron mobility increase by a factor of 4 when the total ion production J_M increases from 50 A/m^2 to 400 A/m^2. It would be interesting to check this scaling experimentally.

When the total ion production rate or current density is too small (below 100 A/m^2 in the present simulations), the anomalous electron mobility due to the fluctuations of the azimuthal field is no longer sufficient to neutralize in a steady way the extracted ion beam. In these conditions, the wave number of the ion acoustic instability in the axial direction increases and axial fluctuations appear. The oscillations observed in the simulations have the characteristics of the transit time oscillations described and been studied in different published papers on Hall thrusters. They propagate at the axial velocity of the ion beam, i.e., typically 15 to 20 km/s. In the present model, they develop between the line of electron emission and the acceleration region (about 1.5 cm) so their frequency is around 1 MHz. These oscillations induce a phase mixing of the ions and therefore a broadening of their energy distribution function. The ion energy distribution function is found to be more beam-like, i.e., more mono-energetic at higher ion current densities.

We have compared results from two different codes and studied the convergence of the results for different grid spacing and as a function of the number of particles per cell. This study tends to show that there is convergence of the results with the number of particles, but it would be useful to run similar simulations with even larger numbers of particles per cell to reduce the numerical noise as much as possible. Another important limitation of the model is the periodicity of the simulation domain in the azimuthal direction. Most of the simulations presented in this paper have been performed with a period of 1 cm in the azimuthal direction. This is much smaller than the length of the azimuthal direction in typical Hall thrusters (e.g., about 30 cm for a 1 kW thruster). It is clear that this small value of the azimuthal period prevents the development or transition to larger instability wavelengths. More systematic simulations for larger azimuthal lengths would therefore be extremely useful to confirm and improve the qualitative and quantitative conclusions of this work.

Although the presence of the $E \times B$ EDI is ubiquitous in PIC simulations including the azimuthal direction under the conditions of Hall thrusters, there is no consensus on its evolution toward a modified ion acoustic instability. Using a highly resolved 1D azimuthal PIC simulation under conditions of Hall thrusters, Janhunen[21] *et al.* showed that the level of turbulence required for the transition to the ion acoustic instability is not reached. They observe a large coherent mode driven mainly at the electron cyclotron drift resonance, and energy flow to long wavelength and low frequency modes. They mention that numerical noise, i.e., "numerical collisions" can destroy the cyclotron resonances and be responsible for the demagnetization associated with the transition to the ion acoustic mode. The results of Janhunen *et al.* must be confirmed under more realistic conditions (i.e., including energy losses or finite length of the acceleration region), but they clearly show the need to validate (or not) the conclusions on the 2D model of the present paper by more systematic studies of the effect of numerical accuracy, noise, and azimuthal periodicity.

ACKNOWLEDGMENTS

[1]D. M. Goebel and I. Katz, *Fundamentals of Electric Propulsion: Ion and Hall Thrusters* (Wiley, 2008).

[2]J.-P. Boeuf, "Tutorial: Physics and modeling of Hall thrusters," J. Appl. Phys. **121**, 011101 (2017).

[3]V. V. Zhurin, H. R. Kaufman, and R. S. Robinson, "Physics of closed drift thrusters," Plasma Sources Sci. Technol. **8**, R1 (1999).

[4]J. C. Adam, A. Héron, and G. Laval, "Study of stationary plasma thrusters using two-dimensional fully kinetic simulations," Phys. Plasmas **11**, 295 (2004).

[5]J. C. Adam, J. P. Boeuf, N. Dubuit, M. Dudeck, L. Garrigues, D. Gresillon, A. Heron, G. J. M. Hagelaar, V. Kulaev, N. Lemoine, S. Mazouffre, J. Perez Luna, V. Pisarev, and S. Tsikata, Plasma Phys. Controlled Fusion **50**, 124041 (2008).

[6]J. Cavalier, N. Lemoine, G. Bonhomme, S. Tsikata, C. Honore, and D. Gresillon, "Hall thruster plasma fluctuations identified as the E x B electron drift instability: Modeling and fitting on experimental data," Phys. Plasmas **20**, 082107 (2013).

[7]T. Lafleur, S. D. Baalrud, and P. Chabert, "Theory for the anomalous electron transport in Hall effect thrusters. II. Kinetic model," Phys. Plasmas **23**, 053503 (2016).

[8]S. Tsikata, N. Lemoine, V. Pisarev, and D. M. Gresillon, "Dispersion relations of electron density fluctuations in a Hall thruster plasma, observed by collective light scattering," Phys. Plasmas **16**, 033506 (2009).

[9]A. Ducrocq, J. C. Adam, A. Héron, and G. Laval, "High-frequency electron drift instability in the cross-field configuration of Hall thrusters," Phys. Plasmas **13**, 102111 (2006).

[10]G. V. Gordeev, Zh. Eksp. Teor. Fiz. **23**, 660 (1952) [Sov. Phys.-JETP **6**, 660 (1952)].

[11]P. S. Gary and J. J. Sanderson, "Longitudinal waves in a perpendicular collisionless plasma shock—I. Cold ions," J. Plasma Phys. **4**, 739 (1970).

[12]D. Forslund, R. Morse, and C. Nielson, "Electron cyclotron drift instability," Phys. Rev. Lett. **25**, 1266 (1970).

[13]D. Forslund, "Electron cyclotron drift instability and turbulence," Phys. Fluids **15**, 1303 (1972).

[14]M. Lampe, W. M. Manheimer, J. B. McBride, J. H. Orens, R. Shanny, and R. N. Sudan, "Nonlinear development of the beam-cyclotron instability," Phys. Rev. Lett. **26**, 1221 (1971).

[15]M. Lampe, W. M. Manheimer, J. B. McBride, J. H. Orens, K. Papadopoulos, R. Shanny, and R. N. Sudan, "Theory and simulation of the beam cyclotron instability," Phys. Fluids **15**, 662 (1972).

[16]J. P. Boeuf, "Rotating structures in low temperature magnetized plasmas—Insight from particle simulations," Front. Plasma Phys. **2**, 74 (2014).

[17]T. Lafleur, S. D. Baalrud, and P. Chabert, "Theory for the anomalous electron transport in Hall effect thrusters. I. Insights from particle-in-cell simulations," Phys. Plasmas **23**, 053502 (2016).

[18]T. Lafleur and P. Chabert, "The role of instability-enhanced friction on 'anomalous' electron and ion transport in Hall-effect thrusters," Plasma Sources Sci. Technol. **27**, 015003 (2017).

[19]J. P. Boeuf, in Proceedings of the 35th International Electric Propulsion Conference, Atlanta, GA (2017).

[20]A. W. Degeling and R. W. Boswell, "Modeling ionization by helicon waves," Phys. Plasmas **4**, 2748 (1997).

[21]S. Janhunen, A. Smolyakov, O. Chapurin, D. Sydorenko, I. Kaganovich, and Y. Raitses, "Nonlinear structures and anomalous transport in partially magnetized E × B plasmas," Phys. Plasmas **25**, 011608 (2018).

[22]J. Boeuf and L. Garrigues, "Low frequency oscillations in a stationary plasma thruster," J. Appl. Phys. **84**, 3541 (1998).

[23]L. Dubois, F. Gaboriau, L. Liard, D. Harribey, C. Henaux, S. Mazouffre, and C. Boniface, "Ion acceleration through a magnetic barrier—Toward an optimized double-stage Hall thruster concept, IEPC-2017-215," in Proceedings of the 35th International Electric Propulsion Conference, Atlanta, GA (2017).

[24]C. K. Birdsall, "Particle-In-Cell charged-particle simulations plus Monte Carlo Collisions with neutral atoms, PIC-MCC," IEEE Trans. Plasma Sci. **19**, 65 (1991).

[25]J. P. Boeuf, B. Chaudhury, and L. Garrigues, "Physics of a magnetic filter for negative ion sources. I. Collisional transport across the filter in an ideal, 1D filter," Phys. Plasmas **19**, 113509 (2012).

[26]J. P. Boeuf, J. Claustre, B. Chaudhury, and G. Fubiani, "Physics of a magnetic filter for negative ion sources. II. E × B drift through the filter in a real geometry," Phys. Plasmas **19**, 113510 (2012).

[27]J. P. Boeuf and B. Chaudhury, "Rotating instability in low-temperature magnetized plasmas," Phys. Rev. Lett. **111**, 155005 (2013).

[28]J. P. Boeuf, G. Fubiani, and L. Garrigues, "Issues in the understanding of negative ion extraction for fusion," Plasma Sources Sci. Technol. **25**, 045010 (2016).

[29]L. Garrigues, G. Fubiani, and J. P. Boeuf, "Negative ion extraction via particle simulation for fusion: Critical assessment of recent contributions," Nucl. Fusion **57**, 014003 (2017).

[30]L. Garrigues, G. Fubiani, and J. P. Boeuf, "Appropriate use of the particle-in-cell method in low temperature plasmas: Application to the simulation of negative ion extraction," J. Appl. Phys. **120**, 213303 (2016).

[31]C. K. Birdsall and A. B. Langdon, *Plasma Physics via Computer Simulation* (Taylor & Francis, Ltd., 2004).

[32]M. K. Scharfe, N. Gascon, and M. A. Cappelli, "Comparison of hybrid Hall thruster model to experimental measurements," Phys. Plasmas **13**, 083505 (2006).

[33]N. Meezan, W. Hargus, and M. Cappelli, "Anomalous electron mobility in a coaxial Hall discharge plasma," Phys. Rev. E **63**, 026410 (2001).

[34]I. Katz, I. G. Mikellides, A. J. Jorns, and A. Lopez-Ortega, EPC-2015-249, in Proceedings of the 34th International Electric Propulsion Conference, Kobe, Japan (2015).

[35]Y. B. Esipchuck and G. Tilinin, Zh. Tekh. Fiz. **46**, 718–729 (1976) [Sov. Phys. Tech. Phys. **21**, 417 (1976)].

[36]Y. B. Esipchuck, A. I. Morozov, G. Tilinin, and A. Trofinov, Sov. Phys. Tech. Phys. **18**, 928 (1974).

[37]S. Barral, K. Makowski, Z. Peradzyński, and M. Dudeck, "Transit-time instability in Hall thrusters," Phys. Plasmas **12**, 073504 (2005).

[38]E. Fernandez, M. K. Scharfe, C. A. Thomas, N. Gascon, and M. A. Cappelli, "Growth of resistive instabilities in E × B plasma discharge simulations," Phys. Plasmas **15**, 012102 (2008).

[39]G. J. M. Hagelaar, J. Bareilles, L. Garrigues, and J. P. Boeuf, "Role of anomalous electron transport in a stationary plasma thruster simulation," J. Appl. Phys. **93**, 67 (2003).